



Performance simulation of solar-driven absorption heat pump-membrane distillation system for combined desalination brine concentration with feed recirculation and cooling applications

Dereje S. Ayou^{*}, Alberto Coronas

Universitat Rovira i Virgili, CREVER-Group of Applied Thermal Engineering, Avda. Països Catalans, 26, 43007, Tarragona, Spain

ARTICLE INFO

Handling editor: Henrik Lund

Keywords:

Absorption heat pump
Membrane distillation
Brine concentration
Feed recirculation
Space cooling
Solar thermal

ABSTRACT

Desalination is the primary choice for securing freshwater provision in water-stressed regions and reduces the gap between rising demand and dwindling natural freshwater resources. However, global desalination plants are dominated by fossil fuel-driven desalination technologies with a 40–50 % recovery ratio. Hence, it is critical to decarbonize desalination and address brine effluent ecological concerns. In this paper, a solar-powered absorption heat pump (AHP)-membrane distillation (MD) system concept was proposed and analysed for small-scale RO plant brine reject management and space cooling applications. The MD subsystem is based on commercial MD modules with batch feed recirculation to reach saturation (from 70 to 260 g/kg salinity). The MD system's heating and cooling consumptions are supplied by the AHP (6.54 MWh and 13.47 MWh, respectively, for a complete batch cycle). The AHP is designed to supply hot water at 85 °C with 701.63 kW heating capacity and co-produced chilled water at 16 °C with a cooling capacity of 857.86 kW, about 67 % is utilized to cool down the brine reject to feed temperature. The thermal and exergy COPs were 1.273 and 0.40 at a driving heat of 135 °C. The solar-powered AHP-MD system is useful for sustainable desalination deployment besides space cooling applications.

Nomenclature

Abbreviations

1, 2, ..., 51	Thermodynamic state points
ABS	Absorber
AGMD	air-gap membrane distillation
AH	auxiliary heater
AHP	absorption heat pump
AHP4SHC	AHP for simultaneous heating and cooling
BP	booster pump
CON	condenser
CP	circulation pump
DES	desorber
EVA	evaporator
HPP	high pressure pump
HX	heat exchanger
MD	membrane distillation
MED	multi-effect desalination
MLD	minimum liquid discharge
MSF	multi-stage flash
PTC	parabolic trough collector

Subscripts

0	dead state
a	ambient or aperture
abs	Absorber
b	final brine
batch	batch cycle
c	cooling or cold
col	collector
con	condenser
cp	circulation pump
des	desorber
el	electrical
eva	evaporator
f	feed
h	heating or hot
high	high
HPP	high pressure pump
hx	heat exchanger
in	inlet

(continued)

PX	pressure exchanger	low	low
REV	refrigerant expansion valve	m	membrane
RHX	refrigerant heat exchanger	MD	membrane distillation
RO	reverse osmosis	out	outlet
SEV	solution expansion valve	p	pump
SHC	simultaneous heating and cooling	px	pressure exchanger
SHX	solution heat exchanger	RO	reverse osmosis
SP	solution pump	ref	refrigerant
SRF	salt rejection factor	rhx	refrigerant heat exchanger
ST	solar thermal	shc	simultaneous heating and cooling
SW	Seawater	shx	solution heat exchanger
SWRO	seawater reverse osmosis	sol	solar or solar collector
TST	thermal storage tank	sp	solution pump
V-AGMD	vacuum-assisted air gap membrane distillation	th	thermal
ZLD	zero liquid discharge	tot	total
Variables and parameters		u	unit

(continued on next column)

(continued on next page)

* Corresponding author.

E-mail address: derejesendeku.ayou@urv.cat (D.S. Ayou).

(continued)

		<i>Superscripts</i>
A	area (m^2)	
COP	coefficient of performance (-)	app approach
Cp	specific heat capacity ($\text{kJ/kg}\cdot\text{K}$)	eva evaporator
E	energy flow (kWh or MWh)	HPP high pressure pump
eCOP	exergy efficiency (-)	in inlet
GOR	gained output ratio (-)	MD membrane distillation
h	specific enthalpy (kJ/kg)	out outlet
j	permeate flux ($\text{L/h}\cdot\text{m}^2$)	pf primary flow
m̄	mass flow rate (kg/s)	pp pinch point
P	pressure (kPa or bar)	RO reverse osmosis
Q̄	heat flow rate (kW)	sf secondary flow
RR	recovery ratio (-)	ss single pass
s	specific entropy ($\text{kJ/kg}\cdot\text{K}$)	st solar thermal
S	salinity (g/L)	<i>Greek symbols</i>
Sal	salinity (g/kg)	η efficiency (-)
SEC	specific energy consumption (kWh or MWh)	ϵ effectiveness (-)
STEC	specific thermal energy consumption (kWh)	ρ fluid density (kg/m^3)
t	temperature ($^\circ\text{C}$)	Δ difference
V̄	volumetric flow rate (m^3/h or L/h)	Σ summation
W̄	electrical or mechanical power (kW)	τ tau
z	ammonia mass fraction (kg/kg)	

1. Introduction

The global freshwater demand is expected to rise significantly over the coming decades due to rapid population growth, economic development, and lifestyle-driven changes in consumption patterns. The United Nations estimates about 4.8–5.7 billion people live in areas that are potentially water-scarce at least one month per year by 2050 [1]. Besides, if current trends of global water consumption, which are driven mainly by the aforementioned causes, will lead to a 40 % deficit in freshwater supplies by 2030 [2]. Also, when combined with dwindling natural freshwater reserves caused by climate change, it is exacerbating global water shortage. Consequently, desalination technologies are required to close the gap between freshwater demand and supply. Even though desalination can deliver more reliable and climate-independent freshwater from saline water resources (e.g., seawater) available in abundance, its wider adoption is limited by the large energy footprint and associated water treatment cost. Particularly, 30–50 % of total water cost comes from energy consumption alone [3–5], which is currently dominated by fossil fuel-driven seawater desalination systems [5]. As the global deployment of desalination plants rises, which is projected to be 200 million m^3/day by the end of 2030, its carbon footprint is expected to reach a considerable level (1–10 kg CO_2/m^3 of desalinated water), which implies a critical need to decarbonize desalination and produce freshwater sustainably [5].

Conventional seawater desalination is advantageous from the economics of scale, which has led to the implementation of large treatment facilities ($>50,000 \text{ m}^3/\text{day}$ [5]) along the coastline accompanied by vast distribution systems that transport seawater to the centralized desalination plant and deliver desalinated water to end user. Recent studies have shown that water delivery costs can even exceed treatment costs, e.g., the pumping electricity cost alone can reach up to 40 % of the desalinated water cost in water-stressed regions [6]. Hence, decentralized desalination concepts have received considerable interest in recent years [5,7]. Moreover, solar desalination is an attractive technological option since water-scarce regions mostly overlap with good solar resources, which is also favoured by the move toward the deployment of decentralized desalination systems, especially for remote communities as stand-alone systems.

At present, reverse osmosis (RO) has become the most energy-efficient and widely adopted seawater (and brackish water) desalination technology [2,8,9]. Conventional seawater RO (SWRO) plant operates at a pressure of 50–70 bar recovering 40–50 % of feed seawater

as desalinated water with the RO brine rejected back into the sea at approximately 60–70 g/kg of salinity [10]. According to operational data of the SWRO plants from the literature, an average worldwide SWRO plant operated at a recovery ratio of 42 % with about 60 bar operating pressure [10]. Furthermore, in the last decade, advances in RO membrane technology have allowed the development of high-pressure RO (HPRO) systems that can operate up to pressures of 120 bar corresponding to RO brine reject salinity of 120 g/kg [10]. However, these HPRO systems are new and have not yet been adopted widely by the desalination industry [10]. Desalination brine reject is commonly discharged into the environment, and it has adverse impacts, especially in the case of inland desalination plants. Further, desalination brine discharge to sea (and ocean) causes disturbance to marine ecosystems. Several brine disposal methods are employed for instance sewer disposal, deep-well injection, evaporation ponds, etc [11,12]. Inland locations face restrictions with surface discharge due to the environmental impact of hypersaline brine whereas deep-well injection has geographic limitations aside from economic and environmental costs. Accordingly, there is a strong driver to pursue zero liquid discharge (ZLD) or minimal liquid discharge (MLD) processes as a brine management strategy for both coastal and inland desalination facilities [13,14]. Also, ZLD and MLD processes can have other useful outcomes, such as increasing water productivity, resource recovery, and/or valorising the produced solids.

Heat pumps have vast potential as sustainable solutions to address the freshwater shortage by integrating with desalination systems thereby increasing energy efficiency. The integration of heat pumps with main desalination processes (i.e., evaporation-, membrane-, and humidification-dehumidification-based desalination) for performance augmentation was reviewed and investigated in the literature [15]. The overview of research studies on the use of heat pumping technologies (both electrical- and thermal-driven heat pumps) with the different types of desalination systems is discussed as follows.

The potential of a transcritical CO₂-based heat pump integrated with a hybrid membrane distillation (MD)-multi-stage flash (MSF) desalination system was investigated for large-scale applications using thermodynamic and environmental analysis [16]. The CO₂ heat pump provides both heating-for-potable water production and possible cooling output which can be utilized for the cooling of the produced potable water or district cooling applications. The study examined six configurations of the integrated CO₂ heat pump-MD-MSF desalination system with various degrees of complexity from simple to complex layouts. When the potential cooling output was utilized, the integrated system outperformed the RO desalination system (i.e., electricity demand was reduced from 9.6 kWh/ m^3 to 3.2 kWh/ m^3) otherwise it is comparable with the modern RO desalination system.

A system integrating a heat pump, multi-effect desalination (MED), and ice storage subsystems was proposed for seawater desalination and ice production [17]. The heat pump provides both required heating and cooling energies for the desalination and ice (and/or chilled water) production. The system's simulated performance was compared with the conventional mechanical vapour compression (MVC) desalination system and air-conditioning system under various scenarios (i.e., based on chosen countries with different freshwater and electricity prices). The obtained simulation results demonstrated that the proposed integrated system is more energy efficient than the conventional systems by about 47.3 % (4.71 kWh/t and 8.94 kWh/t, respectively). Moreover, the integrated system produced more freshwater ($\sim 1734.6 \text{ t/d}$) than the conventional system ($\sim 1680 \text{ t/d}$) and the payback period of the integrated system is shorter by around 34.8 % (3.85 years for the integrated system and 5.9 years for the conventional system).

A multi-function integrated system operating, at least, three modes of operation was proposed and investigated using energy and exergy analysis for freshwater production, cooling, and heating during different seasons [18]. The multi-function system consists of a single-effect H₂O/LiBr absorption heat pump (AHP), a single-effect H₂O/LiBr

absorption refrigeration heat pump (ARHP, which functions as both a refrigeration unit and a heat pump for heating), and a low-temperature multi-effect evaporation (LT-MEE) desalination unit. The system's three modes of operation were a water-refrigeration mode for summer, a water-only mode for spring and autumn, and a water-heating mode for winter; thus, the system was able to meet the demands of different seasons throughout the whole year. It is driven by motive steam with pressure from 1.5 bar to 3.5 bar with the LT-MEE driven by steam (condensation temperature from 58 °C to 72 °C).

A multi-effect evaporation (MEE) desalination system was integrated into a single-stage H₂O/LiBr AHP to obtain the best optimal operation conditions [19]. The system was evaluated using conventional and advanced exergy and exergoeconomic analyses. The optimized MEE-AHP system produces 15,000 m³/d of freshwater with an exergy efficiency of 10.3 % and a total product cost rate of 0.11 \$/s. The optimized system, which is obtained by minimizing overall avoidable cost rates, was able to reduce the total product cost rates by around 33.3 % and increase the exergy efficiency by 4.8 % compared to the base operating conditions of the system.

The MED desalination system energy consumption is reduced using an NH₃/H₂O absorption-compression heat pump with wastewater as a low-temperature heat source [20]. The integrated MED-NH₃/H₂O heat pump produced 5000 t/d of freshwater, and its performance depends on the heat pump operating conditions (absorber and desorber pressures, which are related to temperatures of the supplied heat to the MED process and waste heat source, respectively). The operating conditions at which the system becomes economically profitable were identified based on Net Present Value evaluation, and the absorber pressure <25 bar and desorber temperature >30 °C (at the desorber pressure of 5 bar). The MED-NH₃/H₂O heat pump was competitive compared to RO technology, and the payback period was within 3 years.

The polygeneration schemes involving desalination systems and solar thermal collector technologies have been proposed as effective and promising ways of addressing water scarcity [21–23]. A solar thermal-powered membrane-based polygeneration system for electrical power, cooling, heating, and freshwater production was proposed and evaluated based on a comprehensive multicriteria assessment approach [21]. The polygeneration system comprises an organic Rankine cycle, a Kalina power cycle, an NH₃/H₂O refrigeration system, and a hybrid pressure retarded osmosis (PRO) and forward osmosis (FO) desalination system. The system can produce 3153.6 t/year of freshwater with net electrical power, heating, and cooling outputs of around 3.032 MW, 8 MW, and 0.401 MW, respectively. An NH₃/H₂O-based integrated system was proposed and analysed for the provision of cooling, electrical power, and seawater desalination [22]. The system consists of a Kalina power cycle, an ejector refrigeration cycle, and a multi-stage spray flash evaporation (SFE) desalination system. An energy and economic comparative study was conducted for two polygeneration system configurations driven by solar collector technologies (i.e., evacuated tube collector (ETC) and Linear Fresnel Reflector (LFR)) [23]. The poly-generation system provides domestic hot water, space heating, space cooling (using the absorption chiller), and desalinated water. The first system option is based on ETC and a single-effect H₂O/LiBr absorption chiller; and the second option is based on LFR with a double-effect H₂O/LiBr absorption chiller. The seawater desalination is carried out by the MED process in both options and a biomass-fired auxiliary heater was used. Thus, for the analysed case study, the ETCs were more profitable than LFRs, achieving simple pay-back periods of about 4–5 years.

Based on the above literature overview of prior studies, the following research gaps were identified.

- Previously proposed heat pump integrated desalination systems were mainly focused on energy efficiency improvement and economic profitability of seawater desalination but not on the brine concentration of seawater desalination plants.

- No solar thermal-driven heat pump coupled desalination system for reject brine management has been investigated.
- Although heat pumps are capable of providing heating and cooling simultaneously most heat pumps are integrated with thermal desalination systems for supplying the required driving heat; however, brine concentrate cooling is also needed especially in brine management with feed recirculation.
- Solar-driven NH₃/H₂O absorption heat pumps integrated with thermal desalination systems for decentralized sustainable desalination applications are scarce in the reported literature.

There is thus the need to develop a solar-powered distributed desalination system with brine management to sustainably address the pressing global water scarcity challenges. In this study, a new solar-driven absorption heat pump-membrane distillation (AHP-MD) system concept is proposed for combined seawater RO plant reject brine desalination and space cooling applications. The MD subsystem is driven by low-grade heat released (at 85 °C) from the condenser of the integrated AHP, and it is used for high recovery brine concentration to reach saturation via batch feed recirculation. The MD system is chosen to desalinate hyper-saline brine since the RO systems concentrating brine to a higher salinity (>120 g/kg, e.g., 260 g/kg) do not currently exist in operation due to the high operating pressures required for brine concentration. In addition, MD systems are driven by low-grade heat (<100 °C) while RO units require high-quality energy input in the form of electricity/mechanical work. The AHP used in the proposed system is designed for the co-production of cooling, e.g., for space conditioning applications besides the heating provided to the MD system. This paper is structured as follows. Section 2 describes the layout of the proposed solar-powered AHP-MD system and its components as well as the coupled conventional SWRO plant. Section 3 presents details of the modelling of system components. Then, Section 4 presents and discusses the obtained results of the proposed solar-powered AHP-MD system, and, finally, the paper concludes with a summary of the key findings in Section 5.

2. Solar-powered AHP-MD system: RO brine concentration and cooling applications

Fig. 1 depicts the proposed solar-powered AHP-MD-RO hybrid desalination system concept for sustainable seawater desalination and space cooling applications. The hybrid RO-MD desalination system is designed for decentralized small-scale applications (<1000 m³/day) with MLD or ZLD process for sustainable desalination. The system's main components and subsystems are a single-stage seawater RO plant, a vacuum-assisted air gap membrane distillation (V-AGMD) system (used as the MD brine concentrator in **Fig. 1**), a single-stage NH₃/H₂O AHP for simultaneous heating and cooling supplies (AHP4SHC), solar thermal (ST) subsystem, and brine and permeate tanks for the batch operation of the V-AGMD system. The saturated brine (260 g/kg of salinity) discharge of the MD system is fed to a salt crystallizer to produce salt using state-of-the-art crystallization technology based on multi-effect evaporators [24] or evaporation pond [25].

2.1. Conventional RO desalination plant

The RO desalination plant configuration chosen in this study, shown in **Fig. 1**, was a typical single-stage RO unit arrangement with a circulation pump (CP), a high-pressure pump (HHP), a booster pump (BP), and a pressure exchanger (PX) for energy recovery. After pretreatment, seawater feed (stream 1) enters the RO desalination plant at ambient temperature and pressure. The feed stream from the CP (2), is then split into two streams (3 and 4), a feed stream goes to an HPP (stream 4) and a feed stream to the PX (stream 3). The HPP then pressurizes part of the feed (stream 4 → 6) to a high pressure (P_{RO}^{HPP}), needed to overcome the

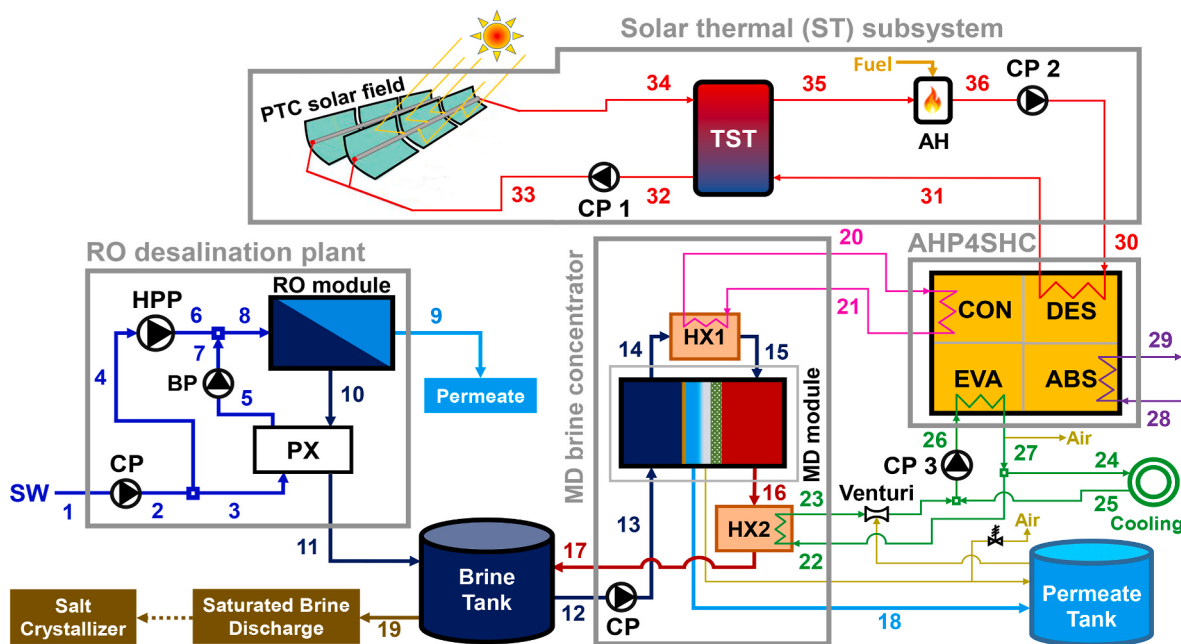


Fig. 1. Solar-powered AHP integrated with MD desalination system with feed brine recirculation for sustainable RO desalination brine concentration and space cooling applications.

osmotic pressure difference, $\Delta\pi$, and pressure losses in the RO module (ΔP_{RO}^{loss}). The other feed stream is pressurized ($3 \rightarrow 5$) by the PX using work produced via the depressurization of brine in the rotor (stream $10 \rightarrow 11$), which is then passed to the BP (stream $5 \rightarrow 7$) to reach the pressure P_{RO}^{HPP} . The two feed streams then combined (i.e., 6 and 7 \rightarrow 8) before entering the RO module and afterward separated into permeate (stream 9) and a concentrated brine stream (10) at a marginally lower pressure due to hydraulic losses. The permeate and concentrate brine reject (leaving the PX, stream 11) from the RO plant feed to permeate and brine tanks at atmospheric pressure, respectively.

2.2. MD brine concentrator with batch feed recirculation

The applied MD subsystem to concentrate the RO plant's reject, stored in the brine tank, is based on a vacuum-assisted air gap membrane distillation module (V-AGMD, type AS26C2.7L) from the Aquastill BV (Netherlands) shown in Fig. 2(a and b). The V-AGMD module uses a

spiral-wound multi-envelope (24 evaporation and cooling channels, 12 for each channel) with a membrane area of 25.92 m^2 , and its internal flow arrangement is illustrated in Fig. 2(c). The AS26 module is used in this simulation study and its technical details are available in Ref. [26]. For the ZLD applications using the MD system, the RO brine reject needs to be concentrated in the range of 232–279 g/L which is an input brine to salt crystallizers while for the MLD the range is between 139 and 167 g/L [27]. To reach saturation from the RO brine reject (e.g., from salinity of 70 g/kg to 260 g/kg) needs a very high recovery ratio of $\sim 73.1\%$ [28].

This is not possible per single pass of the MD module, which can reach up to a 7 % recovery ratio at high feed salinity in the case of the AS26 module [32]. Hence, the batch feed recirculation operational strategy is implemented in the present study, this recirculation mode is chosen since it is more energy efficient than other operational strategies (e.g., continuous recirculation, Refs. [28,33]).

The feed from the brine tank (stream 12) is pumped by the CP and

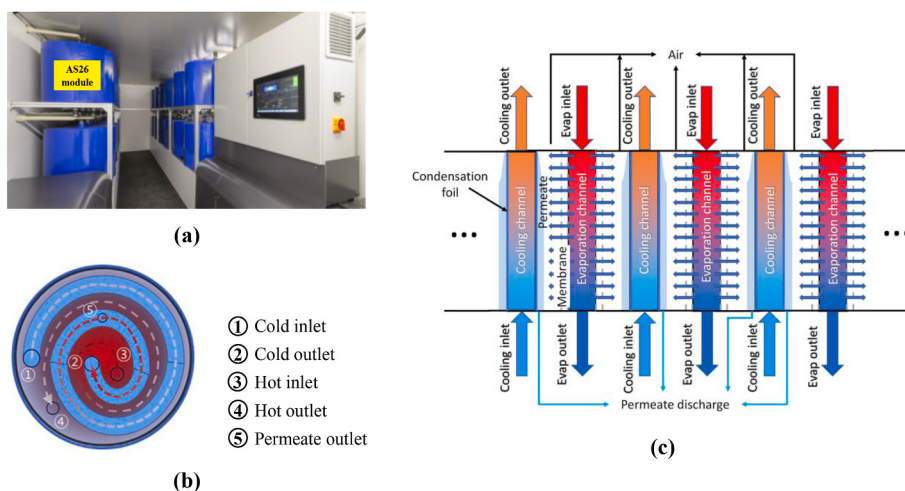


Fig. 2. (a) Aquastill PURA-100 system using AS26 AGMD module, adapted from Ref. [29], (b) cross sectional view of Aquastill AGMD module adapted from Ref. [30], and (c) internal arrangement of a multi-envelope spiral-wound V-AGMD module, adapted from Ref. [31].

preheated in the condenser channels of the MD module (stream 13 → 14). The preheated feed is then heated (stream 14 → 15) in heat exchanger 1 (HX1) to the required evaporator channels inlet temperature using external heat input obtained from the coupled NH₃/H₂O single-stage AHP. The feed solution evaporation (stream 15 → 16) then takes place in the evaporator channels in a counter-current arrangement with flows in the condenser channels. The evaporator outlet stream (16) is returned to the brine storage tank after being cooled down (stream 16 → 17) in the heat exchanger 2 (HX2) using cooling energy produced by the AHP. Finally, the produced distilled water (stream 18) is collected in the permeate storage tank. The brine desalination process (stream 12 → 13 → 14 → 15 → 16 → 17 and 18) is repeated in a batch mode of operation up to the required recovery ratio (i.e., desired final concentrate brine salinity) set for the ZLD (or MLD) applications. Then, the cycle is completed, and the final brine (stream 19) is discharged to a conventional salt crystallizer system (or evaporative pond) in the case of the ZLD; after that, a new batch operation starts and the brine concentration cycle is repeated.

2.3. Absorption heat pump (AHP)

A single-stage AHP cycle using NH₃/H₂O mixture as a working fluid is designed for the delivery of the heating and cooling needs of the MD brine concentrator (i.e., MD subsystem using AS26 module). The single-stage NH₃/H₂O AHP cycle schematic is depicted in Fig. 3 (a) and its representation on the pressure-temperature diagram is shown in Fig. 3 (b).

The AHP comprises four major components that exchange heat with external heat carrier loops: absorber (ABS); condenser (CON); desorber (DES); and evaporator (EVA). The other AHP cycle's components are a rectifier (REC), solution and refrigerant heat exchangers (SHX and RHX), solution and refrigerant expansion valves (SEV and REV), and solution circulation pump (SP). The rectifier is internally cooled by the NH₃-rich solution leaving the absorber prior to entering the solution heat exchanger. The heating output of the AHP (stream 20 → 21) is obtained using the heat released by the condenser while the cooling is provided by the evaporator as shown in Fig. 3. The AHP supplies chilled water (stream 26 → 27, using a circulation pump, CP1, Fig. 1) to the MD subsystem. Depending on the MD brine reject's cooling demand (which is supplied by chilled water stream 22 → 23 in Fig. 1), the remaining chilled water (stream 24 → 25, in Fig. 1) is used for space cooling applications. The driving hot water (stream 30 → 31) produced by the integrated ST plant is provided to the desorber of the absorption heat pump. The absorber rejects heat to the external cooling water loop

(stream 28 → 29), which can be the available saline feed resource (seawater), or ambient air using an indirectly (or directly) air-cooled absorber design.

2.4. Solar thermal (ST) subsystem

The solar thermal collector technology used in this study is a parabolic trough collector (PTC) manufactured by Absolicon Solar Collector AB (Sweden) [34]. The Absolicon T160 PTC with glass covering is shown in Fig. 4. The T160 collector produces hot water in the temperature range of 60 °C–160 °C [35]. The solar thermal subsystem, depicted in Fig. 1, comprises a PTC solar field, a thermal storage tank (TST), an auxiliary heater (AH), and circulation pumps (CP1 and CP2). The CP1 is used to circulate the heat transfer fluid (HTF), water, between the solar collector field and thermal storage tank while the CP2 is utilized for the circulation of the heat transfer fluid between the thermal storage tank and desorber of the absorption heat pump.

3. Modelling methodology

3.1. RO desalination process model

The modelling of the conventional RO desalination process is based on Refs. [10,36,37]. The electrical power consumed by each pump ($\dot{W}_{p,el}^{RO}$) in kW, for the feed CP, HPP, and BP) is given by:

$$\dot{W}_{p,el}^{RO} = \left(\frac{1}{\eta_p} \right) \frac{\dot{m}_p^{RO} (P_{out} - P_{in})}{\rho_f} \quad (1)$$

where \dot{m}_p^{RO} is the mass flow rate (kg/s), P_{in} and P_{out} are the pump inlet and outlet pressures (kPa), η_p pump efficiency (taken as 85 %), and ρ_f is the density (kg/m³) of feed seawater. The pressure increase by the feed CP is set to 1.0 bar. The high pressure needed for the RO plant ($P_6 = P_7 = P_8$, in Fig. 1) is given by Ref. [38]:

$$P_6 = \pi_b + \Delta P_{pinch} + \Delta P_{loss} \quad (2)$$

where ΔP_{pinch} is the terminal hydraulic-osmotic pressure pinch value and set to 10 bar (Ref. [38]), ΔP_{loss} denotes the extra consumed work needed to overcome viscous losses in each RO stage (and its value assumed as 2.0 bar, Ref. [38]), π_b is the osmotic pressure (kPa) at the end of the RO unit, which was obtained using the seawater osmotic pressure correlation available in the literature [39]. Thus, the sum of ΔP_{pinch} and ΔP_{loss} is the required overpressure (i.e. above the osmotic pressure, π_b) of the RO

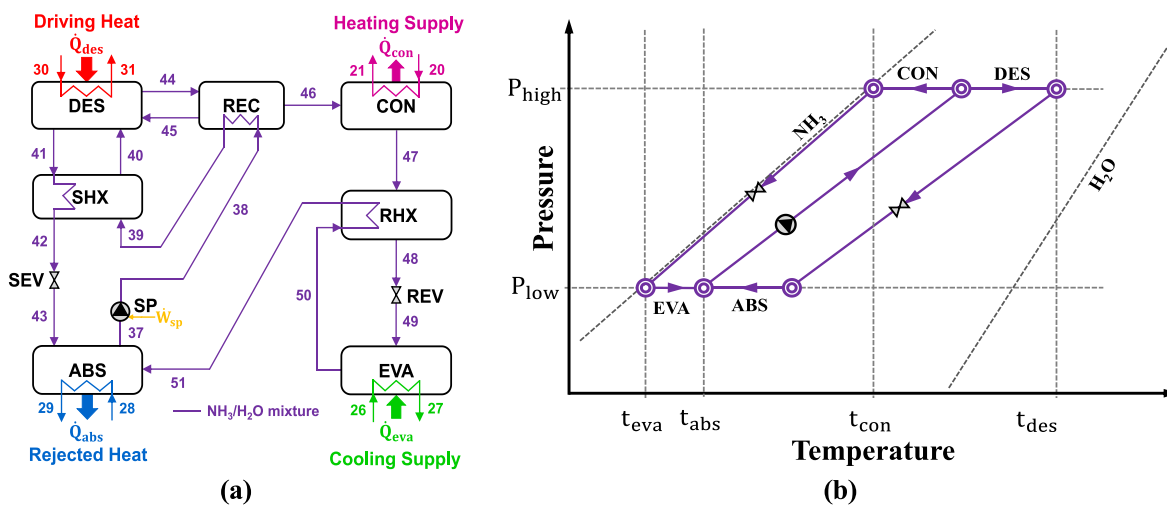


Fig. 3. Single-stage NH₃/H₂O AHP for simultaneous heating and cooling applications (a) cycle schematic and (b) cycle representation on pressure-temperature diagram.

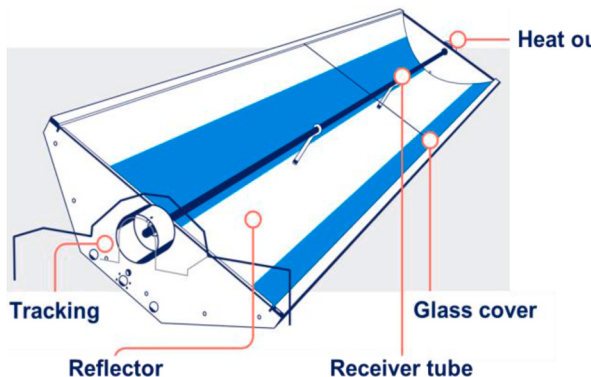


Fig. 4. Absolicon T160 collector with its key component description, adapted from Ref. [34].

stage [40]. The pressure recovered by the PX (P_5 in kPa) of the RO desalination plant is calculated by using Eq. (3).

$$P_5 = P_3 + \eta_{px} \left(\frac{\rho_3}{\rho_{10}} \right) (P_{10} - P_{11}) \quad (3)$$

where η_{px} is the PX efficiency and is taken as 96 % [10]. ρ_3 and ρ_{10} are feed and RO brine concentrate densities in kg/m³, respectively. The feed mass flow rate through the PX (stream 3 → 5, Fig. 1) is assumed equal to the brine mass flow rate through the PX (stream 10 → 11).

The total electrical power consumed, $\dot{W}_{tot,el}^{RO}$ in kW, by the RO desalination plant is:

$$\dot{W}_{tot,el}^{RO} = \dot{W}_{CP,el}^{RO} + \dot{W}_{HPP,el}^{RO} + \dot{W}_{BP,el}^{RO} \quad (4)$$

where $\dot{W}_{CP,el}^{RO}$, $\dot{W}_{HPP,el}^{RO}$, and $\dot{W}_{BP,el}^{RO}$ are electrical power consumed by the CP, HPP, and BP, respectively, computed using Eq. (1). The RO desalination plant performance is estimated by recovery ratio (RR_{RO}) and specific energy consumption (SEC_{RO} in kWh/m³ of produced permeate water) given by Eq. (5) and Eq. (6).

$$RR_{RO} = \frac{\dot{m}_p^{RO}}{\dot{m}_f^{RO}} \quad (5)$$

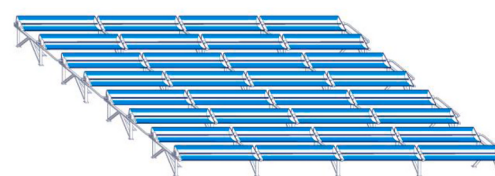
where \dot{m}_p^{RO} is the mass flow rate (kg/s) of permeate water and \dot{m}_f^{RO} is the mass flow rate of feed seawater.

$$SEC_{RO} = \frac{\dot{W}_{tot,el}^{RO}}{\dot{V}_p^{RO}} \quad (6)$$

where \dot{V}_p^{RO} is the permeate water produced in m³/hr.

3.2. Vacuum-assisted AGMD module model

The performance modelling of the commercial V-AGMD module (i.e., Aquastill AS26 module) is based on the statistical model developed by Andrés-Mañas et al. [32] using the AS26 module steady-state operation. The AS26 module was characterized experimentally by Andrés-Mañas et al. at a pilot scale for feed salinity up to 245.5 g/L and then a validated performance model was developed [32]. This model allows to predict the permeate flux (j_{MD} in L/m².hr) and preheated feed brine outlet stream (14, Fig. 1) temperature (T_c^{out}) using experimentally determined correlations given by Eq. (7) and Eq. (8). The average relative errors for the j_{MD} and T_c^{out} , when the experimental data compared with data computed by using the developed correlations, are about 4.2 % and 0.1 %, respectively. Thus, as can be seen from these average relative errors, these correlations yield acceptable deviations. The model validation is carried out for a range of operating conditions: S_f of 35.1–245.5 g/L,



Heat output: provided heat up to 160 °C

Glass cover: Maximized transmittance and lower maintenance

Receiver tube: Converts solar irradiation to heat

Reflector: Focuses the irradiation on the receiver tube

Tracking: Makes the collector follow the sun to maximize performance.

V_f^{MD} of 400–1100 L/h, T_c^{in} of 20–30 °C, and T_h^{in} of 60–80 °C [32].

$$j_{MD} = 0.48 + 0.006 \cdot T_h^{in} - 0.0014 \cdot V_f^{MD} - 0.029 \cdot T_c^{in} + 0.0014 \cdot S_f \\ + 5.3 \cdot 10^{-5} \cdot T_h^{in} \cdot V_f^{MD} - 1 \cdot 10^{-4} \cdot T_h^{in} \cdot S_f - 5 \cdot 10^{-6} \cdot V_f^{MD} \cdot S_f \\ + 1.16 \cdot 10^{-5} \cdot S^2 \quad (7)$$

where T_h^{in} and T_c^{in} are the evaporator and condenser channels inlet temperatures (°C) respectively, S_f is the feed salinity (g/L), and V_f^{MD} is the MD module feed flow rate (stream 12 → 13 → 14 → 15, L/h, in Fig. 1).

$$T_c^{out} = 3.5 + 0.916 \cdot T_h^{in} - 0.0047 \cdot V_f^{MD} + 0.035 \cdot T_c^{in} - 0.01 \cdot S_f \\ + 8 \cdot 10^{-5} \cdot T_c^{in} \cdot V_f^{MD} \quad (8)$$

The produced permeate water (\dot{m}_p^{MD} in kg/s) and specific thermal energy consumption of the MD module ($STEC_{MD}$ in kWh_{th}/m³ of produced permeate water) are given by Eq. (9) and Eq. (10), respectively.

$$\dot{m}_p^{MD} = \left(\frac{1}{3.6 \times 10^6} \right) j_{MD} \cdot A_{MD} \cdot \rho_p \quad (9)$$

where A_{MD} is the membrane area (m²) and ρ_p is the permeate density (kg/m³).

$$STEC_{MD} = \left(\frac{1}{3.6 \times 10^3} \right) \left(\frac{\dot{V}_f^{MD} \cdot C_{pf} \cdot \rho_f \cdot (T_h^{in} - T_c^{out})}{j_{MD} \cdot A_{MD}} \right) \quad (10)$$

where C_{pf} and ρ_f are the feed brine specific heat capacity (kJ/kg · °C) and density (kg/m³), respectively, as a function of S_f and T_h^{in} .

The gained output ratio (GOR) and single-pass permeate water recovery ratio of the MD module (RR_{MD}^{ss}) are given by Eq. (11) and Eq. (12).

$$GOR = h_p^{fg} \frac{j_{MD} \cdot A_{MD} \cdot \rho_p}{\dot{V}_f^{MD} \cdot C_{pf} \cdot \rho_f \cdot (T_h^{in} - T_c^{out})} \quad (11)$$

where h_p^{fg} is the latent heat of the permeate (kJ/kg).

$$RR_{MD}^{ss} = \frac{\dot{m}_p^{MD}}{\dot{V}_f^{MD} \cdot \rho_f} \quad (12)$$

The overall thermal efficiency of the membrane (η_{th}^{MD}) is defined as [41]:

$$\eta_{th}^{MD} = \frac{j_{MD} \cdot A_{MD} \cdot \rho_p \cdot h_p^{fg}}{\dot{V}_f^{MD} \cdot \rho_f \cdot C_{pf} \cdot (T_c^{out} - T_c^{in})} \quad (13)$$

The brine properties are obtained using the correlations of Nayar

et al. [39] and Sharqawy et al. [42]. The electrical power consumption of the MD module's CP ($\dot{W}_{cp,el}^{MD}$ in kW) is calculated by:

$$\dot{W}_{cp,el}^{MD} = \left(\frac{1}{\eta_p} \right) \frac{\dot{m}_f^{MD} \cdot \Delta P_f^{MD}}{\rho_f} \quad (14)$$

where \dot{m}_f^{MD} and ΔP_f^{MD} are the mass flow rate and pressure drop of the MD module brine feed stream.

3.3. AHP cycle model

The AHP model is based on mass and energy conservation laws applied in each component and the overall heat pump cycle. Moreover, the 2nd Law of thermodynamics is ensured in each heat pump component model. The correlations of $\text{NH}_3/\text{H}_2\text{O}$ mixture properties were taken from Tillner-Roth and Friend [43] while properties of water used as an external heat carrier loop were calculated from the IAPWS-IF95 values. The following commonly used AHP cycle modelling assumptions are made [44]: • steady-state conditions are considered; • pressure drops and fluid leakage in pipelines are neglected; • potential and kinetic energy effects are neglected; • no heat losses to the environment; • liquid solution leaving the absorber and desorber are at saturated state at their corresponding temperature and pressure; • the liquid refrigerant leaving the condenser is saturated; • partial vaporization is allowed in the evaporator with fixed temperature glide; • the expansion processes in the solution and refrigerant expansion valves are isenthalpic; • the rectified vapour and liquid reflux leaving the rectifier are saturated; • the solution and refrigerant heat exchangers have a constant effectiveness value; • the solution pump has constant isentropic efficiency (70%).

The AHP performance is evaluated using the coefficient of performance (COP_{shc}) and exergy efficiency ($eCOP_{shc}$) defined for simultaneous heating and cooling supplies and given by Eqs. (15) and (16).

$$COP_{shc} = \frac{\dot{Q}_{con} + \dot{Q}_{eva}}{\dot{Q}_{des}} \quad (15)$$

where \dot{Q}_{con} , \dot{Q}_{des} , and \dot{Q}_{eva} are heat flow rates (kW) of condenser, desorber, and evaporator, respectively.

$$eCOP_{shc} = \frac{\dot{Q}_{con} \cdot \left| \left(1 - \frac{T_0}{\bar{T}_{con}} \right) \right| + \dot{Q}_{eva} \cdot \left| \left(1 - \frac{T_0}{\bar{T}_{eva}} \right) \right|}{\dot{Q}_{des} \cdot \left| \left(1 - \frac{T_0}{\bar{T}_{des}} \right) \right| + \dot{W}_{sp}} \quad (16)$$

where \bar{T}_{con} , \bar{T}_{des} , and \bar{T}_{eva} are the entropic average temperatures of the external heat transfer loop of the condenser (stream 20 → 21), desorber (stream 30 → 31) and evaporator (stream 26 → 27) shown in Fig. 3, respectively, T_0 is the dead state temperature taken as 298.15 K (25 °C) in this study, and \dot{W}_{sp} is the electrical power (kW) consumed by the solution pump.

3.4. ST subsystem modelling

The solar thermal power, $\dot{Q}_{sol,u}$, produced by the PTC solar field (comprising the T160 collectors from the Absolicon solar AB) is determined by applying the quasi-dynamic model:

$$\frac{\dot{Q}_{sol,u}}{A_{sol}} = \eta_{0,b} \cdot (K_{ob}(\theta_L, \theta_T) \cdot G_b + K_{ob} \cdot G_d) - c_1(t_m - t_a) - c_2(t_m - t_a)^2 - c_3 \cdot u(t_m - t_a) + c_4(E_L - \sigma T_a^4) - c_5 \frac{dt_m}{dt} - c_6 \cdot u \cdot G \quad (17)$$

where A_{sol} is the solar collector area (m^2); $\eta_{0,b}$ is the optical (zero loss) efficiency of the collector for beam radiation, at a normal incidence angle (-); θ_L and θ_T are the biaxial incidence angles for beam radiation

onto the collector plane in longitudinal (L) and transversal (T) direction from the normal [°]; G_b the direct beam solar radiation in the collector plane (W/m^2); G_d the diffuse solar radiation in the collector plane; $K_{ob}(\theta_L, \theta_T)$ incidence angle modifier (IAM) for beam solar radiation (-), this can be expressed as $K_{ob}(\theta_L, \theta_T) = K_{ob}(\theta_L) \cdot K_{ob}(\theta_T)$ and $K_{ob}(\theta_T) = 1.0$ for collector tracking the sun with the tracking axis aligned north to south; K_{od} is the IAM for diffuse solar radiation (-), is a collector constant; c_1-c_6 are the solar collector constants (-); u the wind speed (m/s), E_L the long wavelength radiation (W/m^2), and σ is the Stefan-Boltzmann constant ($5.67 \cdot 10^{-8} \text{ W}/\text{m}^2 \text{ K}^4$); t_m is the mean PTC fluid temperature; t_a is the ambient air temperature close to the collector. $K_{ob}(\theta_L)$ is calculated using Eq. (18) and the coefficients of Eq. (17) and Eq. (18) for the T160 solar collector are listed in Table 1. The IAM for beam radiation (i.e., $K_{ob}(\theta_L)$ in Eq. (18)) in the collector test incidence angle values are also given in the Solar Keymark test report [45].

$$K_{ob}(\theta_L) = 1 - b_0 \left(\frac{1}{\cos \theta_L} - 1 \right) \quad (18)$$

where b_0 is the incidence angle modifier coefficient (-).

The useful heat rate from the PTC solar field ($\dot{Q}_{sol,u}$ in kW) can be calculated using:

$$\dot{Q}_{sol,u} = \dot{m}_{sol} \cdot C_{p,sol} \cdot (t_{34} - t_{33}) \quad (19)$$

where \dot{m}_{sol} is the mass flow rate (kg/s) of the primary solar loop (stream 32 → 33 → 34, Fig. 1), $C_{p,sol}$ is the specific heat capacity of water at collector mean temperature, t_{33}/t_{34} are the inlet/outlet temperatures (streams 33/34) of the PTC solar field.

The thermal efficiency of the PTC solar field ($\eta_{col,th}$) is defined as:

$$\eta_{col,th} = \frac{\int \dot{Q}_{sol,u}}{A_{sol} \cdot \int G_b} \quad (20)$$

where G_b is the direct beam radiation (kW/m^2).

The storage tank simulation is based on mixing zones modelling by dividing the tank volume into zones with an assumed uniform temperature level. The electrical power consumed by the ST subsystem's circulation pumps (CP1 and CP2), $\dot{W}_{cp1,el}^{ST}$ and $\dot{W}_{cp2,el}^{ST}$, are calculated as:

$$\dot{W}_{cp1,el}^{ST} = \left(\frac{1}{\eta_{cp1}^{ST}} \right) \frac{\dot{m}_{sol} \cdot (P_{33} - P_{32})}{\rho_{32}} \text{ and } \dot{W}_{cp2,el}^{ST} = \left(\frac{1}{\eta_{cp2}^{ST}} \right) \frac{\dot{m}_{36} \cdot (P_{30} - P_{36})}{\rho_{36}} \quad (21)$$

where η_{cp1}^{ST} and η_{cp2}^{ST} are the CP1 and CP2 efficiency, $(P_{33} - P_{32})$ and $(P_{30} - P_{36})$ is the pressure rise by the pumps, ρ_{32} and ρ_{36} the density of water at the inlet of CP1 and CP2 (streams 32 and stream 36), and \dot{m}_{36} is the mass flow rate (kg/s) of the secondary water loop (stream 35 → 36 → 30 → 31). The pressure drops in the PTC collector, ΔP_{col} in mbar at 20 °C, is calculated by Ref. [46]:

Table 1
PTC performance model parameters and coefficients of Eq. (17) and Eq. (18) based on collector aperture area [45,46].

Parameter/Coefficient (unit)	Value
Zero loss efficiency of the collector for beam radiation, $\eta_{0,b}$ (-)	0.7661
Incidence angle modifier for diffuse radiation, K_{od} (-)	0.08586
Heat loss coefficient, c_1 ($\text{W}/\text{m}^2 \cdot \text{K}$)	0.3677
Temperature dependent heat loss coefficient, c_2 ($\text{W}/\text{m}^2 \cdot \text{K}^2$)	0.003224
Wind speed-dependent heat loss coefficient, c_3 ($\text{W}/\text{m}^2 \cdot \text{K}$)	0.000
Coefficient for sky temperature-dependent radiative heat losses, a_4 (-)	0.000
Effective thermal capacitance, c_5 ($\text{J}/(\text{m}^2 \cdot \text{K})$)	1629
Coefficient for wind dependence of zero loss efficiency, c_6 (s/m)	0.000
Incidence angle modifier coefficient, b_0 (-)	0.210
Collector aperture area, $A_{col,a}$ (m^2)	5.5
Collector test flow rate, $\dot{V}_{col,test}$ (l/s)	0.28

$$\Delta P_{col} = 14.334 \cdot \dot{V}_{col}^2 + 8.260 \cdot \dot{V}_{col} \quad (22)$$

where \dot{V}_{col} is the heat transfer fluid (water) flow rate in m^3/h .

The secondary loop of the ST subsystem is heated to the desired temperature ($t_{36} = t_{AH, set}$, Fig. 1) using an auxiliary heater when the available solar energy is inadequate ($t_{36} < t_{AH, set}$). The amount of heat delivered to the desorber of the absorption heat pump via the auxiliary heater, \dot{Q}_{AH} in kW, is given by:

$$\dot{Q}_{AH} = \eta_{AH} \cdot \dot{m}_{sf} \cdot LHV_{fuel} - UA_{AH} \cdot (t_m - t_a) = \dot{m}_{sf} \cdot Cp_{sf} \cdot (t_{AH, set} - t_{35}) \quad (23)$$

where η_{AH} and UA_{AH} are the auxiliary heater's thermal efficiency (–) and heat loss coefficient (kW/K).

The solar fraction (SF) of the ST-AHP-MD system with an auxiliary heater is defined as:

$$SF = 1 - \frac{\int \dot{Q}_{AH}}{\int \dot{Q}_{des}} \quad (24)$$

where the \dot{Q}_{des} is the driving heat consumed by the absorption heat pump (i.e. desorber heat rate, \dot{Q}_{des}). The dynamic simulation of the ST-AHP system was carried out using TRNSYS software [47], and details of the system's component TRNSYS model (type) are given in Appendix A. The weather data of Almería (Spain), from the EnergyPlus database [48], were used in this study. A simulation time step of 5 min and convergence tolerance of 0.001 were set during the system simulation performed for 8760 h of the year.

The proposed solar-powered AHP-MD-RO system input modelling parameters and operating conditions at the reference case, and their variation ranges for the parametric analysis, are listed in Table 2.

4. Results and discussion

In this section, the performance simulation results of the proposed solar-powered AHP-MD-RO system are presented. In Section 4.1 the performance of the hybrid RO-MD desalination system is presented and

Table 2

Input modelling parameters and operating conditions for the performance analysis of the solar-powered AHP-MD-RO system (Fig. 1).

Parameter and unit	Value (range)
Feed seawater (stream 1)	
Temperature, t_1 (°C)	19.1 ^a
Pressure, P_1 (bar)	1.0
Salinity, Sal (g/kg)	40 ^b
RO-MD desalination subsystem	
RO desalination plant capacity, V_p^{RO} (m^3/day)	100 [49]
HX 1 and HX 2 terminal temperature difference, ΔT_{hx1} and ΔT_{hx2} (°C)	5.0 and 4.0
Salt rejection factor of SWRO plant, SRF_{RO} (%)	99.6 (99.4–99.7) ^b
Concentrate brine reject salinity of RO plant, Sal_b^{RO} (g/kg)	70 [50]
V-AGMD module feed flow rate, V_f^{MD} (L/h)	1100
Efficiency of MD circulation pump, η_{cp}^{MD} (%)	
Single-stage NH₃/H₂O AHP cycle	
NH ₃ mass fraction of rectified vapour, z_{ref} (kg/kg)	0.9995
EVA temperature glide, t_{glide}^{eva} (K)	2.5
Approach temperature difference, ΔT_u^{app} (°C)	5/5/8/3
ABS/CON/DES/EVA	8.0
DES pinch point temperature difference, ΔT_{des}^{pp} (°C)	90
Effectiveness of SHX and RHX, ϵ_{shx} and ϵ_{rhx} (%)	20 (20–35)/ t_{28} + 6
ABS cooling water inlet/outlet temperatures, t_{28}/ t_{29} (°C)	21/16
Chilled water inlet/outlet temperatures, t_{26}/ t_{27} (°C)	85

^a yearly average seawater temperature of Almería (Spain) [51] and seawater salinity for Almería (Spain) considering the salinity of the Mediterranean Sea (~40 g/kg [52], 38–41 g/kg [53]).

^b SRF (Salt Rejection Factor) for standard SWRO system [54].

in Section 4.2 the integrated AHP performance is provided. Finally, in Section 4.3, the annual performance of the solar-powered AHP-MD system is presented for the chosen location (Almería, Spain).

4.1. RO-MD desalination subsystem

The small-scale RO desalination plant process (100 m^3/day freshwater production capacity) is operating at a recovery rate, RR_{RO} , of 43.0 % with SEC_{RO} of about 2.316 kWh/m³ in the reference case considered for Almería (Spain). The corresponding electrical power consumed by the RO plant process, $W_{tot,el}^{RO}$ calculated using Eq. (4), is ~ 9.65 kW_{el}. Besides, there is additional energy consumption for pre-treatment (0.65 kWh/m³) and post-treatment, which is often neglected in contrast to other energy consumption, processes of the RO desalination plant [52, 55]. The required RO plant feed pressure is ~ 66.1 bar. The amount of brine concentrate rejected by the RO plant is 126 m^3/day , which is fed to the brine storage tank. The feed seawater temperature (stream 1, Fig. 1) has a significant impact on the design of the RO plant feed pressure (HPP) and membrane performance [56]. For instance, the osmotic pressure increased from 53.3 bar to 57.9 bar when seawater temperature increased from 15 °C to 40 °C at 40 g/kg of salinity. The HPP required for the SWRO plant is typically reduced linearly by 5 – 8 % for every 10 °C rise in the feed temperature (from 12 °C to 40 °C) [56].

The single-pass MD system performance using the Aquastill AS26 AGMD module is depicted in Fig. 5 for feed brine salinity up to saturation. The performance parameters (permeate flow rate \dot{V}_p^{MD} , recovery ratio RR_{MD}^{ss} , GOR , and $STEC_{MD}$) were obtained based on J_{MD} and T_c^{out} computed using the correlations given by Eq. (7) and Eq. (8), respectively. The values of J_{MD} is reduces from 2.676 L/h·m² to 0.860 L/h·m² and T_c^{out} slightly decreases from 73.4 °C to 72.1 °C when the feed salinity increased from 70 g/kg to 260 g/kg.

In Fig. 6 (a), the overall thermal efficiency of the membrane (η_{th}^{MD}), calculated using Eq. (13), and feed preheating rate in the condenser/cooling channels (\dot{Q}_{con}^{MD}) are shown for the MD system operated with a single pass of the feed brine. The η_{th}^{MD} and \dot{Q}_{con}^{MD} are obtained at the feed flow rate of 1100 L/h and 25.92 m² membrane area. The external heat input rate (\dot{Q}_{hx1}^{MD}) and required cooling input rate (\dot{Q}_{hx2}^{MD}) to cool down the brine reject, to 20 °C, of the MD system per single pass of the feed brine are depicted in Fig. 6 (b). The required flow rate of the MD system's driving hot water (stream 21 → 20, HX1, Fig. 1) at 85 °C, per single-pass of feed brine solution (1100 L/h), is reduced from around 1292.3 L/h to 1032.3 L/h when the salinity increased from 70 g/kg to 260 g/kg. While the flow rate of chilled water (i.e., stream 22 → 23, HX2, Fig. 1) at 16 °C is between about 1052.3 L/h and 1275.7 L/h with the maximum flow rate at 190–195 g/kg of salinity. The electrical power consumed by the feed pump of the MD subsystem, per single-pass, is increased from 0.017 kW to 0.020 kW when the salinity increased from 70 g/kg to 260 g/kg.

The MD subsystem's performance and operating parameters in batch mode of operation are defined and presented in Table 3. The instantaneous performance of the MD system is captured by using the developed steady-state model of the commercial V-AGMD module in Section 3.2, and the simulated performance at instantaneous feed salinity is depicted in Figs. 5 and 6. It is supposed that the external brine feed tank is large enough so that the rate of change in salinity is slow during the system operation. The required total cycle time for a batch operation (τ_{batch}), i.e., from the feed solution salinity of $Sal_f = 70$ g/kg way up to saturation at $Sal_b = 260$ g/kg, is evaluated using Eq. (25). The average permeate flux, GOR , and $STEC$ (\bar{J}_{MD} , \bar{GOR} , and \bar{STEC} , respectively) given in Table 3 are independent of the initial mass of the feed brine solution ($M_{MD,f}^{total}$); thereby, they are independent of the feed tank volume. The external driving heat input and cooling input rates (\dot{Q}_h and \dot{Q}_c , respectively) are also independent of the size of the feed tank volume. However, large feed tank volume is supposed for the quasi-steady approximation made

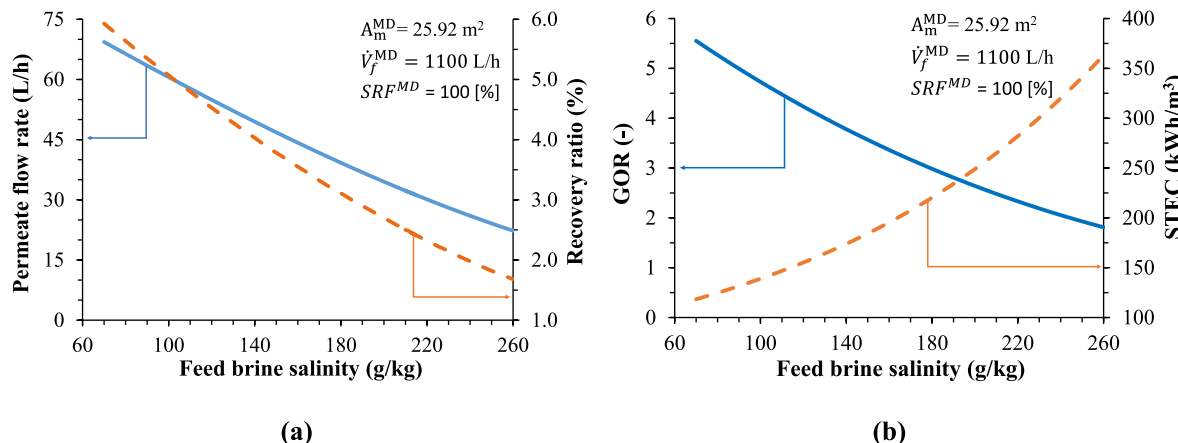


Fig. 5. Effect of feed brine salinity for a single-pass MD system based on Aquastill AS26 AGMD module on (a) permeate production rate and recovery ratio and (b) GOR and STEC.

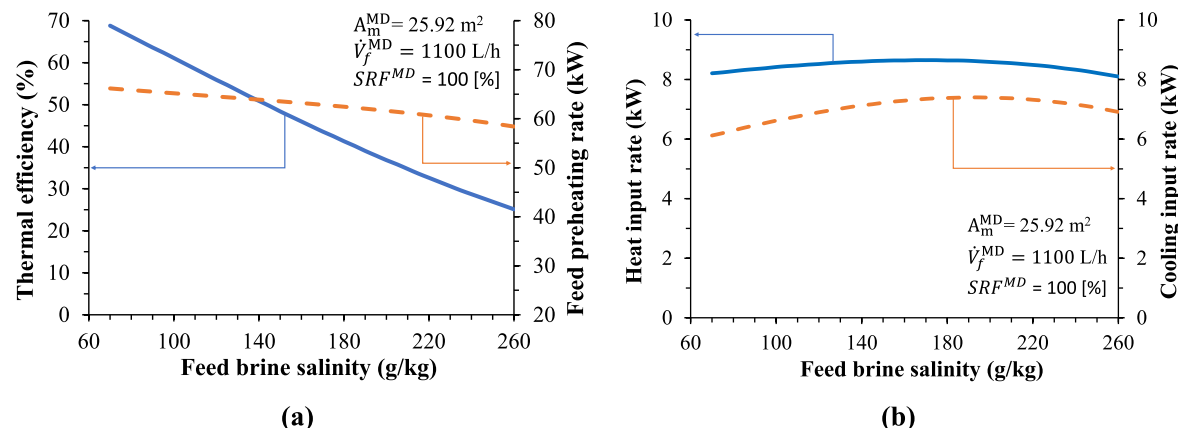


Fig. 6. Effect of feed brine salinity for a single-pass MD system using the Aquastill AS26 AGMD module on (a) thermal efficiency and condenser channels preheating rate and (b) external heat input and cooling input rates.

during the batch operation of the MD subsystem and the impact of transients between the batch operations can be neglected. Also, the hydrophobic membrane wetting phenomena and scaling with the use of high salinity feeds (70–260 g/kg) should be investigated for the long-term operation of the MD subsystem as an RO brine concentrator. Consequently, there are various methods proposed in the literature for pre-treating brine rejects of seawater RO plants including the use of antiscalant, chemical deposition combined with ultrafiltration (UF), and nanofiltration (NF) [57]. Thus, it has been shown that the problem of scaling with high salinity feeds can be prevented using, e.g., antiscalants for an air-gap MD system under lab- and pilot-scale operations [57].

The MD subsystem performance for the concentration of the RO plant's reject (i.e., 126 m³/day at 70 g/kg salinity) is presented in Table 4. At the reference conditions listed in Table 1 and per batch operation of the MD modules, the system delivers around 97.9 m³ of desalinated water with around 29.8 m³ of concentrated brine reject at 260 g/kg of salinity and 20 °C. The required number of the V-AGMD modules (i.e., 83) was estimated based on the average permeate flux of ~ 1.909 L/h·m² while the minimum required module number (59) corresponds to the maximum permeate flux (2.676 L/h·m²). The MD subsystem operates at an average GOR of 3.888 and STEC of 169 kWh/m³ over the cycle time (i.e., $\tau_{batch} = 23.6$ h). The heating and cooling consumed by the MD subsystem are 16.54 MWh and 13.47 MWh, respectively at an average heating and cooling input rates of 701.6 kW and 571.2 kW supplied by the integrated heat pump.

4.2. AHP performance

The solar-powered NH₃/H₂O AHP is integrated into an MD subsystem as illustrated in Fig. 1 for the supply of simultaneous heating and cooling demand of the MD system. Thereby, computed performance parameters of the AHP during the simultaneous heating and cooling supplies (COP_{shc} and $eCOP_{shc}$) at reference conditions (Table 2) are presented in Fig. 7 (a) and 7 (b).

The AHP cycle is designed to provide the required heating rate (\dot{Q}_h) for the MD subsystem, which is 701.63 kW at a hot water supply temperature (t_{21}) of 85 °C. The simultaneous cooling output (\dot{Q}_c) of the AHP cycle was 857.86 kW at a chilled water supply temperature (t_{27}) of 16 °C and around 67 % of this cooling output is used for cooling down the MD brine reject to 20 °C before returning to the brine storage tank (stream 16 → 17, Fig. 1). The remaining cooling output (i.e., 286.69 kW) is available for space cooling applications (stream 24 → 25). The AHP's stream properties at the reference conditions, given in Table 2, and the driving heat temperature (t_{30}) corresponding to the optimum performance are presented in Table 5. The AHP cycle operates at high- and low-pressure levels of 49.98 and 6.81 bar.

The effect of driving heat source temperature (t_{30} , between 120 °C and 160 °C) on the desorber and absorber heat transfer rates are also illustrated in Fig. 8(a) and (b), respectively, at several absorber's cooling water inlet temperatures (i.e., 20 °C, 25 °C, 30 °C, and 35 °C). The AHP operates at high performance ($COP_{shc} = 1.273$ and $eCOP_{shc} = 0.40$, at a driving heat of 135 °C) when seawater at 20 °C is used as the absorber's

Table 3

Equations for performance and operating parameters of the MD subsystem evaluation under the batch process conditions.

Parameter	Equation
τ_{batch} (h)	$\frac{1000 \cdot M_{MD,f}^{tot} \cdot Sal_f}{N^{MD} \cdot A_m^{MD} \cdot \rho_p} \cdot \int_{Sal_f}^{Sal_b} \frac{1}{Sal^2 \cdot J(Sal)} dSal \quad (25)$
\bar{J}_{MD} (L/h·m ²)	$\frac{\rho_p \cdot \left(\frac{1}{Sal_f} - \frac{1}{Sal_b} \right)}{1000 \cdot \int_{Sal_f}^{Sal_b} \frac{1}{Sal^2 \cdot J(Sal)} dSal} \quad (26)$
GOR (-)	$\bar{h}_{fg} \cdot \frac{A_m^{MD} \cdot \rho_p \cdot \left(\frac{1}{Sal_f} - \frac{1}{Sal_b} \right)}{3.6 \cdot 10^6 \cdot \int_{Sal_f}^{Sal_b} \frac{Q_{hx1}(Sal)}{Sal^2 \cdot J(Sal)} dSal} \quad (27)$
$STEC$ (kWh/m ³)	$\frac{Q_f^h}{V_{MD,p}^{total}} = \frac{1}{3600} \cdot \frac{\bar{h}_g \cdot \rho_p}{GOR} \quad (28)$
\bar{Q}_h (kW)	$\frac{Q_f^h}{\tau_{batch}} \quad (29)$
\bar{Q}_c (kW)	$\frac{Q_f^h}{\tau_{patch}} \quad (30)$
E_h^h (kWh)	$\frac{1000 \cdot M_{MD,f}^{tot} \cdot Sal_f}{\rho_p \cdot A_m^{MD}} \int_{Sal_f}^{Sal_b} \frac{Q_{hx1}(Sal)}{Sal^2 \cdot J(Sal)} dSal \quad (31)$
E_c^h (kWh)	$\frac{1000 \cdot M_{MD,f}^{tot} \cdot Sal_f}{\rho_p \cdot A_m^{MD}} \int_{Sal_f}^{Sal_b} \frac{Q_{hx2}(Sal)}{Sal^2 \cdot J(Sal)} dSal \quad (32)$
V_p^{MD} (m ³)	$\frac{M_{MD,f}^{tot} \cdot \left(1 - \frac{Sal_f}{Sal_b} \right)}{\rho_p} \quad (33)$

$M_{MD,f}^{tot}$ = initial feed brine mass (kg). N^{MD} = number of MD module (#). A_m^{MD} = membrane area of MD module (m²). ρ_p = average permeate density (989.6 kg/m³). Sal = salinity (g/kg). Sal_f = feed brine salinity (70 g/kg). Sal_b = final brine salinity (260 g/kg). \bar{h}_{fg} = average permeate enthalpy of vaporization (2390.79 kJ/kg).

Table 4

Performance summary of the MD subsystem (RO plant brine concentrator in Fig. 1) based on V-AGMD module (type AS26C2.7L, Aquastill BV) at the reference conditions (Table 2).

Parameter	Value
Batch cycle time, τ_{batch} (h)	23.6
Cooling energy consumed, E_c^h (MWh)	13.467
Cooling capacity, \bar{Q}_c (kW)	571.17
Heating energy consumed, E_h^h (MWh)	16.543
Heating capacity, \bar{Q}_h (kW)	701.63
Gained output ratio, GOR (-)	3.888
Permeate flux, \bar{J}_{MD} (L/h·m ²)	1.909
Permeate water produced, V_p^{MD} (m ³)	97.88
Minimum number of modules, N_{MD}^{min} (#)	59
Number of modules, N_{MD} (#)	83
Specific thermal energy consumption, $STEC$ (kWh/m ³)	169.02

heat rejection medium (stream 28 → 29, Fig. 1). The NH₃ mass fraction difference across the solution field of the AHP cycle ($\Delta z = z_s - z_w$) is 0.1275 kg/kg with strong (basic) and weak, in NH₃, solution mass fractions of 0.7153 kg/kg and 0.5878 kg/kg, respectively. The power consumed by the solution pump is about 23.31 kW at the considered reference condition.

4.3. Annual performance analysis

The ST-AHP-MD system's annual performance was simulated considering different sizes of the ST field to reach at least 20 % solar fraction each month of the year using Almería (Spain) weather data. Fig. 9 depicts the effect of ST field aperture area on the solar fraction, calculated using Eq. (24), during the whole year. The yearly solar

fraction is ~ 22.3 % for 990 m², 32.2 % for 1980 m², 42.1 % for 3025 m², and 50.7 % for 4015 m².

The produced useful heat by the ST field is about 1120 MWh/year, 2209.07 MWh/year, 3301.19 MWh/year, and 4270 MWh/year for the considered ST field aperture area of 990 m², 1980 m², 3025 m², and 4015 m², respectively. There are 10 solar PTC collectors per row in each simulated ST field. The yearly thermal efficiency of the PTC collectors, calculated using Eq. (20), is about 63.9 % for 990 m², 63 % for 1980 m², 61.6 % for 3025 m², and 60.1 % for 4015 m². The yearly available direct beam, sky diffuse, and ground-reflected diffuse solar radiation on the collector surface is 1770.49 kWh/m², 606.25 kWh/m², and 42.89 kWh/m², respectively; and their monthly variation along the year is given in Fig. 10. The annual average, minimum, and maximum ambient air temperatures ($t_{a,avg}$, $t_{a,min}$, and $t_{a,max}$) are 18.5 °C, 2.8 °C, and 35 °C; and their variation also shown in Fig. 10.

Based on the simulated ST-AHP-MD system performance (Fig. 9), the ST field with an aperture area of 1980 m² (i.e. 360 Absolicon T160 collectors) was considered as a reference case to attain a minimum of 20 % solar fraction every month of the year. The system's solar fraction, computed using Eq. (24), varied between ~ 19.8 % (December) and 43.6 % (July) for the 1980 m² ST field aperture area. The ST field's produced useful heat and thermal efficiency, output heat of the auxiliary heater, and desorber heat input (i.e. AHP driving heat input) are presented for each month of the year in Fig. 11. The delivered heat by the ST field is between 72.25 MWh (December) and 309 MWh (July) with thermal efficiency in the range of 52.5 % (December) to 66.4 % (July). The direct beam radiation is in the range of 69.52 kWh/m² (December) and 234.86 kWh/m² (July). The auxiliary heater provided about 7161.1 MWh/year of heat to complement the heat supplied by the PTC solar collectors. Thus, the driving heat supplied to the AHP is 10561.6 MWh/year. The primary (solar) loop circulation pump (CP1, Fig. 1) is controlled during the system operation using a hysteresis controller that uses the ST field inlet and outlet temperatures and the thermal storage tank top outlet temperature to monitor for a high cut-off limit (details given in Appendix A). The secondary loop circulation pump (CP2) and auxiliary heater operation are controlled based on the AHP operation schedule.

The heating and cooling outputs of the AHP are depicted in Fig. 12 for each month throughout the year. The temperature range of seawater used as the absorber heat rejection medium (stream 28, Fig. 3(a)) is also shown in Fig. 12 (SW min and SW max values [58]). The AHP provided about 6146.28 MWh/year of heating and 7514.85 MWh/year of cooling simultaneously with 21 h/d of operational schedule (~ 88 % yearly plant availability). The calculated combined COP of the AHP, using Eq. (15), is between 1.201 (August) and 1.371 (February).

Since the AHP cycle is designed to deliver the required heat of the MD subsystem all the heat pump's heating output is utilized to desalt the RO brine reject (i.e., the heating output shown in Fig. 12 is used by the MD brine concentrator). The MD brine concentrator's cooling need is also provided by part of the co-produced cooling output of the AHP (67 % of the cooling output is consumed by the MD brine concentrator). The annual produced permeate and remaining cooling output (which may be used for space cooling applications) of the proposed system are given monthly in Fig. 13. The MD brine concentrator produced 31260.43 m³/year of desalinated water and rejected brine concentrate of 9517.38 m³/year (at 260 g/kg of salinity).

5. Conclusions

A solar-powered NH₃/H₂O absorption heat pump (AHP)-membrane distillation (MD) system concept was proposed and investigated for RO brine reject management and space cooling applications. The AHP-MD system is used to concentrate rejected brine of an RO desalination plant with 100 m³/day capacity from 70 g/kg to 260 g/kg of salinity. The employed MD system is based on commercial vacuum-assisted air gap membrane distillation modules (V-AGMD) with feed recirculation in

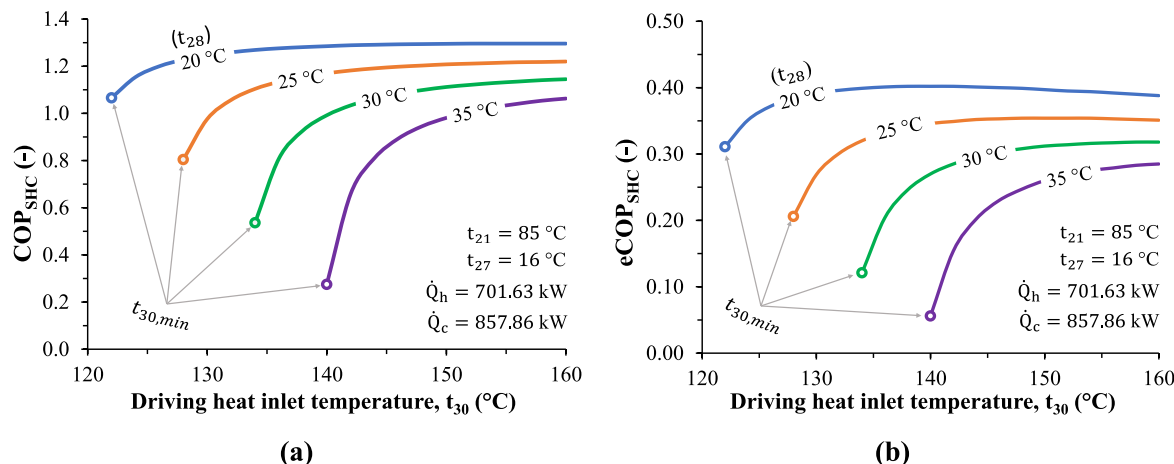


Fig. 7. Effect of AHP driving heat temperature (t_{30}) at several absorber cooling water inlet temperatures (t_{28}) on (a) COP and (b) eCOP for simultaneous heating and cooling supplies.

Table 5

Stream properties of the AHP for simultaneous heating and cooling (Fig. 3 (a)) at the reference conditions (Table 2) and driving heat temperature of 135 °C.

Stream (i)	t_i (°C)	p_i (kPa)	z_i (kg/kg)	\dot{m}_i (kg/s)	h_i (kJ/kg)	s_i (kJ/kg-K)
20	79	200	–	27.855	330.94	1.064
21	85	200	–	27.855	356.13	1.135
26	21	200	–	40.998	88.28	0.311
27	16	200	–	40.998	67.36	0.239
28	20	101.3	–	58.911	79.21	0.279
29	26	101.3	–	58.911	102.98	0.359
30	135	322.4	–	13.809	567.75	1.687
31	114.1	322.4	–	13.809	479.01	1.464
37	25	680.9	0.7153	2.775	167.78	1.276
39	26.1	4998	0.7153	2.775	176.18	1.285
39	35.6	4998	0.7153	2.775	221.75	1.435
40	92.9	4998	0.7153	2.775	506.35	2.279
41	127	4998	0.5878	1.915	584.46	2.477
42	44.8	4998	0.5878	1.915	172.17	1.326
43	38.1	680.9	0.5878	1.915	172.17	1.345
44	110.6	4998	0.9887	0.893	1714.23	5.408
45	110.6	4998	0.7153	0.034	600.15	2.530
46	90	4998	0.9995	0.859	1611.20	5.126
47	88.9	4998	0.9995	0.859	794.70	2.871
48	57.2	4998	0.9995	0.859	619.71	2.366
49	13	680.9	0.9995	0.859	619.71	2.444
50	15.5	680.9	0.9995	0.859	1618.02	5.932
51	81.6	680.9	0.9995	0.859	1793.01	6.481

batch mode of operation. The heating and cooling energies consumed by the MD subsystem were about 16.54 MWh and 13.47 MWh, respectively, over a complete batch cycle (23.6 h). These heating and cooling demands are delivered by the integrated AHP capable of providing hot

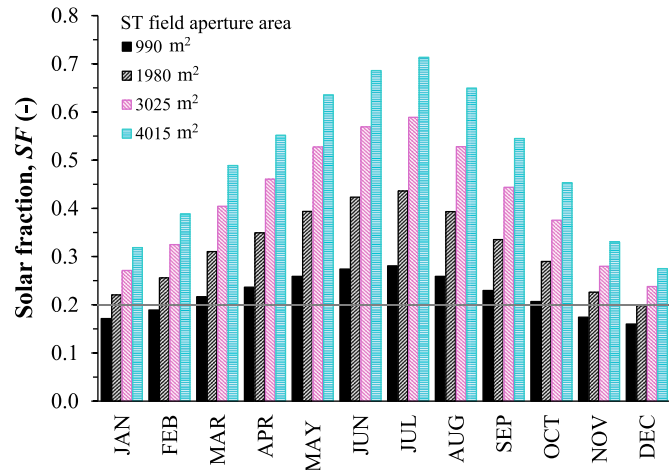


Fig. 9. Effect of solar field area on the solar fraction of the ST-AHP-MD system with auxiliary heater.

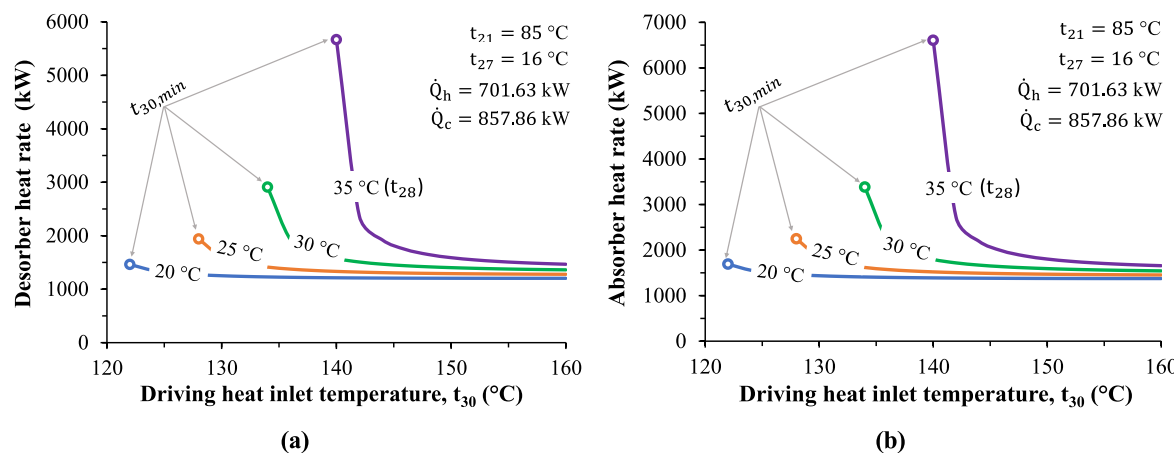


Fig. 8. Effect of driving heat temperature (t_{30}) at several absorber cooling water temperatures (t_{28}) on (a) desorber heat rate and (b) absorber heat rate of the AHP for simultaneous heating and cooling supplies.

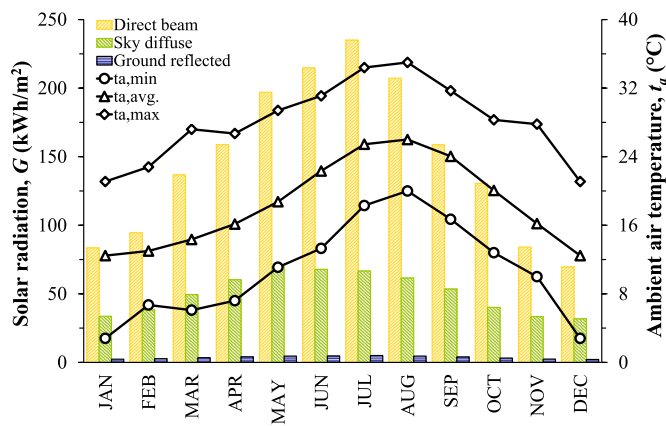


Fig. 10. Monthly variation of solar radiation and ambient air temperature of Almería (Spain) [48].

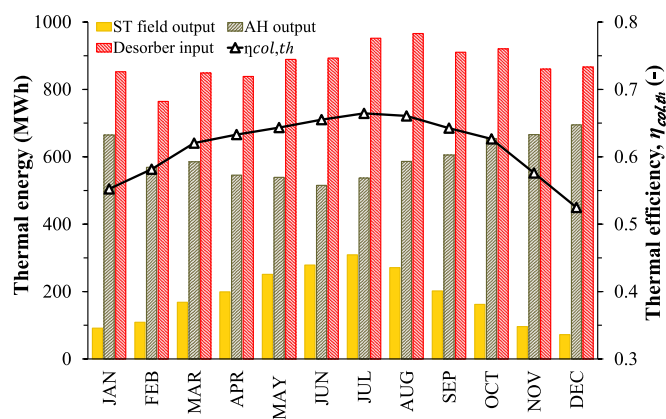


Fig. 11. ST field useful heat output and thermal efficiency, auxiliary heater (AH) output heat, and desorber heat input monthly variation of the ST-AHP-MD system (ST field of 1980 m² aperture area).

water and chilled water at 85 °C and 16 °C simultaneously. The AHP heating capacity is 701.63 kW, and its co-produced cooling capacity is about 857.86 kW of which ~ 67 % is used for cooling down the MD system's brine reject to the feed storage tank temperature (20 °C). The AHP operates at a thermal combined COP (COP_{shc}) and exergy COP ($eCOP_{shc}$) of 1.273 and 0.40, respectively, when the AHP is driven by hot water at 135 °C and absorber heat rejection medium (seawater) temperature of 20 °C. The proposed solar-powered AHP-MD system with an auxiliary heater operates at a monthly solar fraction between ~19.8 % (December) and 43.6 % (July) for a considered solar field aperture area of 1980 m² using Almería (Spain) weather conditions. The system produced about 31260.43 m³/year of desalinated water (and rejected brine concentrate of about 9517.38 m³/year at 260 g/kg of salinity) and 2511.40 MWh/year of cooling energy for space cooling applications. In summary, the development of small-scale solar-powered AHP-MD systems for RO desalination plant brine management (for both coastal and inland desalination facilities) contributes towards the development of sustainable zero liquid discharge (ZLD) or minimal liquid discharge

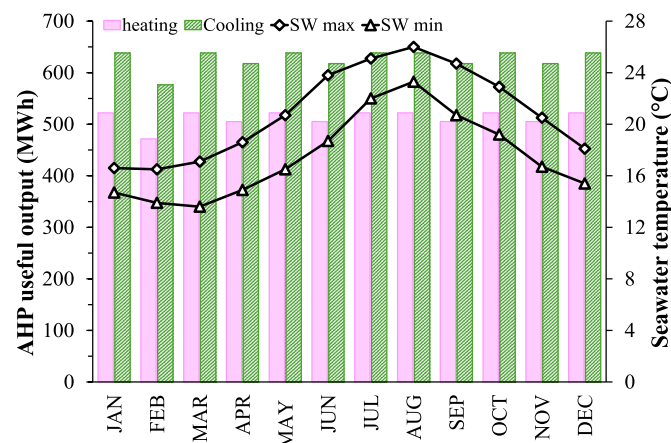


Fig. 12. Monthly absorption heat pump (AHP) simultaneous heating and cooling outputs and seawater temperature range of Almería (Spain).

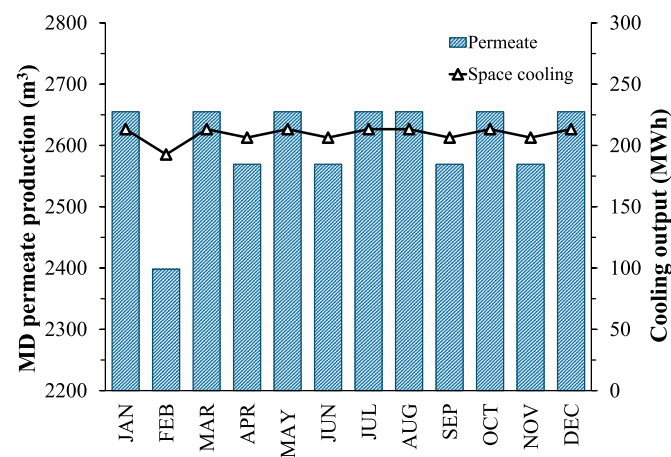


Fig. 13. Monthly permeate production and cooling output-for-space cooling applications of the proposed ST-AHP-MD system with auxiliary heater.

(MLD) desalination processes besides other (space) cooling applications.

CRediT authorship contribution statement

Dereje S. Ayou: Writing – review & editing, Writing – original draft, Software, Methodology, Investigation, Formal analysis, Conceptualization. **Alberto Coronas:** Supervision, Resources, Funding acquisition, Conceptualization.

Declaration of competing interest

The authors declare that they have no known competing financial interests or personal relationships that could have appeared to influence the work reported in this paper.

Appendix A. Description of component/utility and corresponding TRNSYS types used for the simulated ST-AHP system integrated with an MD brine concentrator (Fig. 1)

Component/utility	TRNSYS Model	Remark
Weather ST collector field	Type 15-3	file type: EPW (EnergyPlus Weather); tracking mode: 3 (single-axis tracking E-W); azimuth: 0° (southward orientation)
	Type 1288	dynamic simulation of the solar PTC field using Absolicon T160 collector with its coefficients/parameters (listed in Table 1) obtained according to ISO 9806:2013 quasi dynamic test method [45,46]. The collector test incidence angle values are given in the Solar Keymark test report [45]
Thermal Storage Tank (TST)	Type 4c	stratified hot water tank, and its volume (V_{TST}) is calculated as $A_{sol}/30$ [59]; tank height: 2.5 m; temperature levels (nodes): 10; auxiliary heater rate: 0 W; heat loss coefficient: 0.7 W/m ² ·K; boiling point temperature: 180 °C (water)
Auxiliary heater (AH)	Type 6	setpoint temperature ($t_{AH,se}$): 140 °C; maximum heating rate: 1500 kW; thermal efficiency: 0.9; overall heat loss coefficient: 8.3 W/K; controlled by the AHP schedule
Absorption heat pump (AHP)	Equation	modelled using correlations obtained from the AHP performance simulation data; constant simultaneous heating (701.63 kW at 85 °C) and cooling (857.86 kW at 16 °C) supplies; external heat carrier loop constant flow rates (Fig. 3(a)): $m_{21} = 27.855 \text{ kg/s}$, $m_{22} = 40.998 \text{ kg/s}$, $m_{23} = 58.911 \text{ kg/s}$, and $m_{30} = 13.809 \text{ kg/s}$; absorber heat rejection medium (seawater) inlet temperature: ~ 14–26 °C (Almería, Spain [58]); desorber driving heat stream inlet temperature: 140–160 °C; ~ 88 % operational availability
Circulation Pump 1 (CP1)	Type 110	variable speed pump; rated flow rate (\dot{m}_{sol}): 0.02 · A_{sol} [59]; overall efficiency: 0.6; motor efficiency: 0.9; rated power: calculated using the PTC collector pressure loss (calculated using Eq. (22) with temperature correction) and pump's efficiency
Circulation Pump 2 (CP2)	Type 114	constant speed pump controlled by the AHP schedule (based on MD concentrator operation); rated flow rate (\dot{m}_{sf}): 13.809 kg/s; overall efficiency: 0.6; motor efficiency: 0.9; rated power: calculated using $\Delta P_{cp2} = 100 \text{ kPa}$ and pump efficiency
Controller	Type 2b	used to control CP1 operation using the lower limit set for solar radiation ($G = 10 \text{ W/m}^2$); upper dead band: 1 °C; lower dead band: 0.5 °C; high limit cut-out temperature: 180 °C
Quantity integrator	Type 24	integration period for the monthly simulation outputs: -1; integration period for annual simulation outputs: 8760 h
Output printer	Type 25c	export simulation results to an Excel file

Data availability

Data will be made available on request.

References

- [1] UNESCO. Nature-based solutions for water. The United Nations World Water Development Report 2018:1–154.
- [2] Deshmukh A, Boo C, Karanikola V, Lin S, Straub AP, Tong T, et al. Membrane distillation at the water-energy nexus: limits, opportunities, and challenges. Energy Environ Sci 2018;11:1177–96. <https://doi.org/10.1039/c8ee00291f>.
- [3] Bank World. Renewable energy desalination: an emerging solution to close the water gap in the Middle East and north Africa. Washington DC, <https://doi.org/10.1596/978-0-8213-8838-9>; 2012.
- [4] Al-Karaghoubi A, Kazmerski LL. Energy consumption and water production cost of conventional and renewable-energy-powered desalination processes. Renew Sustain Energy Rev 2013;24:343–56. <https://doi.org/10.1016/j.rser.2012.12.064>.
- [5] Menon AK, Jia M, Kaur S, Dames C, Prasher RS. Distributed desalination using solar energy: a techno-economic framework to decarbonize nontraditional water treatment. iScience 2023;26:105966. <https://doi.org/10.1016/j.isci.2023.105966>.
- [6] Caldera U, Bogdanov D, Breyer C. Chapter 8 - desalination costs using renewable energy technologies. In: Gude VG, editor. Renewable energy powered desalination handbook. Butterworth-Heinemann; 2018. p. 287–329. <https://doi.org/10.1016/B978-0-12-815244-7.00008-8>.
- [7] Mauter MS, Fiske PS. Desalination for a circular water economy. Energy Environ Sci 2020;13:3180–4. <https://doi.org/10.1039/d0ee01653e>.
- [8] Bouma AT, Lienhard JH. Split-feed counterflow reverse osmosis for brine concentration. Desalination 2018;445:280–91. <https://doi.org/10.1016/j.desal.2018.07.011>.
- [9] Jones E, Qadir M, van Vliet MTH, Smakhtin V, mu Kang S. The state of desalination and brine production: a global outlook. Sci Total Environ 2019;657:1343–56. <https://doi.org/10.1016/j.scitotenv.2018.12.076>.
- [10] Nayar KG, Fernandes J, McGovern RK, Dominguez KP, McCance A, Al-Anzi BS, et al. Cost and energy requirements of hybrid RO and ED brine concentration systems for salt production. Desalination 2019;456:97–120. <https://doi.org/10.1016/j.desal.2018.11.018>.
- [11] Ogunbiyi O, Sathivasivam J, Al-Masri D, Manawi Y, Lawler J, Zhang X, et al. Sustainable brine management from the perspectives of water, energy and mineral recovery: a comprehensive review. Desalination 2021;513:115055. <https://doi.org/10.1016/j.desal.2021.115055>.
- [12] Voutchkov N. Overview of seawater concentrate disposal alternatives. Desalination 2011;273:205–19. <https://doi.org/10.1016/j.desal.2010.10.018>.
- [13] Prado de Nicolás A, Molina-García Á, García-Bermejo JT, Vera-García F. Desalination, minimal and zero liquid discharge powered by renewable energy sources: current status and future perspectives. Renew Sustain Energy Rev 2023;187:113733. <https://doi.org/10.1016/j.rser.2023.113733>.
- [14] Panagopoulos A. Brine management (saline water & wastewater effluents): sustainable utilization and resource recovery strategy through Minimal and Zero Liquid Discharge (MLD & ZLD) desalination systems. Chemical Engineering and Processing - Process Intensification 2022;176:108944. <https://doi.org/10.1016/jcep.2022.108944>.
- [15] Liu H, Joseph A, Elsayad MM, Elshernoby B, Awad F, Elsharkawy M, et al. Recent advances in heat pump-coupled desalination systems: a systematic review. Desalination 2022;543. <https://doi.org/10.1016/j.desal.2022.116081>.
- [16] Petersen NH, Arras M, Wirsum M, Ma L. Integration of large-scale heat pumps to assist sustainable water desalination and district cooling. Energy 2024;289. <https://doi.org/10.1016/j.energy.2023.129733>.
- [17] Chen L, Liu X, Ye K, Xie M, Lan W. Thermodynamic and economic analysis of an integration system of multi-effect desalination (MED) with ice storage based on a heat pump. Energy 2023;283. <https://doi.org/10.1016/j.energy.2023.129064>.
- [18] Wang Y, Morosuk T, Yang S, Cao W. A high-efficiency multi-function system based on thermal desalination and absorption cycle for water, water-cooling or water-heating production. Energy Convers Manag 2023;284. <https://doi.org/10.1016/j.enconman.2023.116962>.
- [19] Janghorban Esfahani I, Lee SC, Yoo CK. Evaluation and optimization of a multi-effect evaporation-absorption heat pump desalination based conventional and advanced exergy and exergoeconomic analyses. Desalination 2015;359:92–107. <https://doi.org/10.1016/j.desal.2014.12.030>.
- [20] Li H, Russell N, Sharifi V, Swithenbank J. Techno-economic feasibility of absorption heat pumps using wastewater as the heating source for desalination. Desalination 2011;281:118–27. <https://doi.org/10.1016/j.desal.2011.07.049>.
- [21] Moosazadeh M, Tariq S, Safder U, Yoo CK. Techno-economic feasibility and environmental impact evaluation of a hybrid solar thermal membrane-based power desalination system. Energy 2023;278. <https://doi.org/10.1016/j.energy.2023.127923>.
- [22] Zhou S, Liu X, Zhang K, Yue Q, Bian Y, Shen S. Evaluation of a novel ammonia-water based combined cooling, desalination and power system based on thermodynamic and exergoeconomic analyses. Energy Convers Manag 2021;239. <https://doi.org/10.1016/j.enconman.2021.114176>.
- [23] Calise F, Dentice d'Accadia M, Vanoli R, Vicidomini M. Transient analysis of solar polygeneration systems including seawater desalination: a comparison between linear Fresnel and evacuated solar collectors. Energy 2019;172:647–60. <https://doi.org/10.1016/j.energy.2019.02.001>.
- [24] Chung HW, Nayar KG, Swaminathan J, Chehayeb KM, Lienhard JH. Thermodynamic analysis of brine management methods: zero-discharge desalination and salinity-gradient power production. Desalination 2017;404:291–303. <https://doi.org/10.1016/j.desal.2016.11.022>.
- [25] Ayou DS, Ega HM, Coronas A. A feasibility study of a small-scale photovoltaic-powered reverse osmosis desalination plant for potable water and salt production in Madura Island: a techno-economic evaluation. Therm Sci Eng Prog 2022;35:101450. <https://doi.org/10.1016/j.tsep.2022.101450>.
- [26] Andrés-Manas JA, Requena I, Ruiz-Aguirre A, Zaragoza G. Performance modelling and optimization of three vacuum-enhanced membrane distillation modules for up-scaled solar seawater desalination. Sep Purif Technol 2022;287:120396. <https://doi.org/10.1016/j.seppur.2021.120396>.
- [27] Zhang Z, Atia AA, Andrés-Manas JA, Zaragoza G, Fthenakis V. Comparative techno-economic assessment of osmotically-assisted reverse osmosis and batch-operated vacuum-air-gap membrane distillation for high-salinity water

- desalination. Desalination 2022;532:115737. <https://doi.org/10.1016/j.desal.2022.115737>.
- [28] Swaminathan J, Lienhard JH. Design and operation of membrane distillation with feed recirculation for high recovery brine concentration. Desalination 2018;445: 51–62. <https://doi.org/10.1016/j.desal.2018.07.018>.
- [29] Aquastill. Datasheet PURA-100 system 2020:1–2. <https://www.aquastill.nl/cms/wp-content/uploads/AKA-ASL-Papers-Data-Pilot-Pura-100.pdf>. [Accessed 10 July 2024].
- [30] Lee CK, Park C, Woo YC, Choi JS, Kim JO. A pilot study of spiral-wound air gap membrane distillation process and its energy efficiency analysis. Chemosphere 2020;239:124696. <https://doi.org/10.1016/j.chemosphere.2019.124696>.
- [31] Andrés-Mañas JA, Requena I, Zaragoza G. Characterization of the use of vacuum enhancement in commercial pilot-scale air gap membrane distillation modules with different designs. Desalination 2022;528:115490. <https://doi.org/10.1016/j.desal.2021.115490>.
- [32] Andrés-Mañas JA, Requena I, Zaragoza G. Membrane distillation of high salinity feeds: steady-state modelling and optimization of a pilot-scale module in vacuum-assisted air gap operation. Desalination 2023;553:116449. <https://doi.org/10.1016/j.desal.2023.116449>.
- [33] Bindels M, Brand N, Nelemans B. Modeling of semibatch air gap membrane distillation. Desalination 2018;430:98–106. <https://doi.org/10.1016/j.desal.2017.12.036>.
- [34] Absolicon Solar Collector AB. Absolicon T160 collector. <https://www.absolicon.com/applying-absolicon/>. [Accessed 10 July 2024].
- [35] Saini P, Ghasemi M, Arpagaus C, Bless F, Bertsch S, Zhang X. Techno-economic comparative analysis of solar thermal collectors and high-temperature heat pumps for industrial steam generation. Energy Convers Manag 2023;277:116623. <https://doi.org/10.1016/j.enconman.2022.116623>.
- [36] Thiel GP, Tow EW, Banchik LD, Chung HW, Lienhard VJH. Energy consumption in desalinating produced water from shale oil and gas extraction. Desalination 2015; 366:94–112. <https://doi.org/10.1016/j.desal.2014.12.038>.
- [37] Mistry KH, McGovern RK, Thiel GP, Summers EK, Zubair SM, Lienhard JH. Entropy generation analysis of desalination technologies. Entropy 2011;13:1829–64. <https://doi.org/10.3390/e13101829>.
- [38] Nayar KG, Fernandes J, McGovern RK, Al-Anzi BS, Lienhard JH. Cost and energy needs of RO-ED-crystallizer systems for zero brine discharge seawater desalination. Desalination 2019;457:115–32. <https://doi.org/10.1016/j.desal.2019.01.015>.
- [39] Nayar KG, Sharqawy MH, Banchik LD, Lienhard JH. Thermophysical properties of seawater: a review and new correlations that include pressure dependence. Desalination 2016;390:1–24. <https://doi.org/10.1016/j.desal.2016.02.024>.
- [40] Lin S, Veerapaneni S. Emerging investigator series: toward the ultimate limit of seawater desalination with mesopelagic open reverse osmosis. Environ Sci 2021;7: 1212–9. <https://doi.org/10.1039/D1EW00153A>.
- [41] Andrés-Mañas JA, Ruiz-Aguirre A, Acién FG, Zaragoza G. Performance increase of membrane distillation pilot scale modules operating in vacuum-enhanced air-gap configuration. Desalination 2020;475:114202. <https://doi.org/10.1016/j.desal.2019.114202>.
- [42] Sharqawy MH, Lienhard VJH, Zubair SM. Thermophysical properties of seawater: a review of existing correlations and data. Desalination Water Treat 2010;16: 354–80. <https://doi.org/10.5004/dwt.2010.1079>.
- [43] Tillner-Roth R, Friend DG. A helmholtz free energy formulation of the thermodynamic properties of the mixture {water + ammonia. J Phys Chem Ref Data 1998;27:63–94.
- [44] Herold KE, Radermacher R, Klein SA. Absorption chillers and heat pumps. Second. Boca Raton: CRC Press, Inc.; 2016.
- [45] SPF. Annex to solar Keymark certificate - summary of EN ISO 9806 test results for concentrating collector, licence number: 011-S2902 C, date issued: 2019-02-07, issued by: DIN CERTCO 2019:1-2. http://www.solarkeymark.nl/DBF/PDF_Download/DS_2013.pdf. [Accessed 14 July 2024].
- [46] Absolicon. T160 solar collector datasheet 2021:1–2. https://www.absolicon.com/wp-content/uploads/2021/06/05_T160-Solar-Collector_Datasheet.pdf. [Accessed 14 July 2024].
- [47] TRNSYS 17. A transient system simulation program. Software. Version: 5.4.0.0. Copyright (C) 2009–2012.
- [48] EnergyPlus. Almeria (Spain) weather data. https://energyplus.net/weather-location/europe_wmo_region_6/ESP/ESP_Almeria.084870_SWEC. [Accessed 22 May 2024].
- [49] Song J, Li T, Wright-Contreras L, Law AWK. A review of the current status of small-scale seawater reverse osmosis desalination. Water Int 2017;42:618–31. <https://doi.org/10.1080/02508060.2017.1330841>.
- [50] Tong T, Elimelech M. The global rise of zero liquid discharge for wastewater management: drivers, technologies, and future directions. Environ Sci Technol 2016;50:6846–55. <https://doi.org/10.1021/acs.est.6b01000>.
- [51] Ayou DS, Zaragoza G, Coronas A. Small-scale renewable polygeneration system for off-grid applications: desalination, power generation and space cooling. Appl Therm Eng 2021;182:116112. <https://doi.org/10.1016/j.applthermaleng.2020.116112>.
- [52] Palenzuela P, Alarcón-Padilla DC, Ortega-Delgado B, Zaragoza G. Cogeneration of fresh water and electricity with high-temperature power cycles: comparative assessment of multi-effect distillation and reverse osmosis. Processes 2023;11. <https://doi.org/10.3390/pr11041181>.
- [53] Greenler LF, Lawler DF, Freeman BD, Marrot B, Moulin P. Reverse osmosis desalination: water sources, technology, and today's challenges. Water Res 2009; 43:2317–48. <https://doi.org/10.1016/j.watres.2009.03.010>.
- [54] Okamoto Y, Lienhard JH. How RO membrane permeability and other performance factors affect process cost and energy use: a review. Desalination 2019;470: 114064. <https://doi.org/10.1016/j.desal.2019.07.004>.
- [55] Pearce GK. UF/MF pre-treatment to RO in seawater and wastewater reuse applications: a comparison of energy costs. Desalination 2008;222:66–73. <https://doi.org/10.1016/j.desal.2007.05.029>.
- [56] World Bank. The role of desalination in an increasingly water-scarce world. DC; 2019. <https://doi.org/10.1596/31416>.
- [57] Bindels M, Carvalho J, Gonzalez CB, Brand N, Nelemans B. Techno-economic assessment of seawater reverse osmosis (SWRO) brine treatment with air gap membrane distillation (AGMD). Desalination 2020;489. <https://doi.org/10.1016/j.desal.2020.114532>.
- [58] World sea temperature. Almería sea temperature. <https://www.seatemperature.org/europe/spain/almera.htm>. [Accessed 16 June 2024].
- [59] Bellos E, Tzivanidis C, Antonopoulos KA. Exergetic and energetic comparison of LiCl-H₂O and LiBr-H₂O working pairs in a solar absorption cooling system. Energy Convers Manag 2016;123:453–61. <https://doi.org/10.1016/j.enconman.2016.06.068>.